

## Original Article

# A Liquid Metal Encapsulation for Analyzing Porous Nanomaterials by Atom Probe Tomography

Se-Ho Kim<sup>1,†</sup>, Ayman A. El-Zoka<sup>1,†</sup> and Baptiste Gault<sup>1,2,\*</sup> 

<sup>1</sup>Max-Planck-Institut für Eisenforschung, Düsseldorf, Germany and <sup>2</sup>Department of Materials, Royal School of Mines, Imperial College London, London, UK

### Abstract

Analyzing porous (nano)materials via atom probe tomography has been notoriously difficult. Voids and pores act as concentrators of the electrostatic pressure, which results in premature specimen failure, and the electrostatic field distribution near voids leads to aberrations that are difficult to predict. In this study, we propose a new encapsulating method for porous samples using a low melting point Bi–In–Sn alloy, known as Field’s metal. As a model material, we used porous iron made by direct-hydrogen reduction of single-crystalline wüstite. The complete encapsulation was performed using *in situ* heating on the stage of a scanning electron microscope. No visible corrosion nor dissolution of the sample occurred. Subsequently, specimens were shaped by focused ion-beam milling under cryogenic conditions at  $-190^{\circ}\text{C}$ . The proposed approach is versatile and can be applied to provide good quality atom probe datasets from micro/porous materials.

**Key words:** atom probe tomography, fusible alloy, liquid metal, porous iron

(Received 14 March 2021; revised 31 August 2021; accepted 1 October 2021)

### Introduction

Atom probe tomography (APT) provides 3D compositional (Miller & Forbes, 2009; Larson et al., 2013; Gault et al., 2021), and sometimes crystallographic information (Gault et al., 2012) from a material’s microstructure with sub-nanometer resolution (De Geuser & Gault, 2020; Jenkins et al., 2020). To enable field evaporation, the material of interest must be shaped into a sharp needle with a uniform geometry and a radius of curvature in the range of 100 nm at the tip. However, not all materials of interest are fully consolidated or solid. Many recent studies have sought to apply APT to porous materials (El-Zoka et al., 2017; Mouton et al., 2017; Barroo et al., 2019), nanoparticles (Li et al., 2014; Yang et al., 2019; Lim et al., 2020), and materials with cracks (Meisnar et al., 2015) or voids (Wang et al., 2020). Leaving these pores and cracks open introduces stress concentrators that make specimen preparation difficult and complicate the reconstruction of the analyzed specimens due to trajectory aberrations and premature fractures during analysis (Pfeiffer et al., 2015). To deal with this problem, the APT community has established the elimination of these pores/voids/cracks using foreign chemical methods, for instance, electrodeposition (El-Zoka et al., 2018a; Kim et al., 2020), electron beam-induced deposition (Barroo et al., 2020), atomic layer deposition (Larson et al., 2015), organic polymer resin deposition (Perea et al., 2016), and other

physical or chemical vapor deposition methods (Felfer et al., 2014, 2015; Taylor et al., 2019).

Although the surface of sputter-coated samples appears dense, this process cannot penetrate and efficiently fill voids within porous materials. Chemical vapor deposition from C-containing materials typically leads to nonhomogeneous field-evaporation conditions and highly complex mass spectra due to carbon-containing molecular ions (Nishikawa et al., 2006; Prosa et al., 2010). The key challenge in designing a pore infiltration approach is devising a method that does not alter the chemistry and/or structure of the original material while ensuring maximum pore infiltration. This could be difficult for metals that tend to corrode or dissolve due to their relative reactivity, such as iron. The electrodeposition methods reported previously, with materials such as Cu and Ni from sulfate solutions, work for noble metal materials such as Au (El-Zoka et al., 2018b), Pt (El-Zoka et al., 2018c), and Pd (Kim et al., 2018). However, with a reactive metal such as iron, electrodeposition of Cu and Ni will more likely result in dissolution of Fe due to galvanic replacement (Kim et al., 2018), or lead to the formation of FeS on the surfaces during the negative polarization of the sample (Lyon, 2010).

Herein, we demonstrate the use of BiSnIn, a low melting point alloy known as Field’s metal, for infiltrating porous Fe samples formed by direct hydrogen-gas reduction of a single iron oxide crystal. We drew inspiration from a previous report that demonstrated that the re-deposition of a fusible alloy enables the embedding of freestanding nanoparticles (Kim et al., 2019), and we devised a suitable infiltration method for porous transition metals. We used a heating stage inside the scanning electron microscope

<sup>†</sup>These authors contributed equally to this work as co-first authors.

\*Corresponding author: Baptiste Gault, E-mail: [b.gault@mpie.de](mailto:b.gault@mpie.de)

Cite this article: Kim S-H, El-Zoka AA, Gault B (2022) A Liquid Metal Encapsulation for Analyzing Porous Nanomaterials by Atom Probe Tomography. *Microsc Microanal* 28, 1198–1206. doi:10.1017/S1431927621012964

(SEM) to heat up the Field's metal and filled micron-sized pores inside of the FeO sample with the molten metal. Then, we used a cryogenically cooled stage during the focused ion beam (FIB) milling of a needle-shaped specimen suitable for atom probe from the Fe-Field metal composite. Cryo-FIB has recently proven advantageous for avoiding the ingress of Ga (Dantas De Moraes et al., 2014; Lilensten & Gault, 2020), preserving specimen's compositions (Chang et al., 2019; Rivas et al., 2020), and preparing APT specimens from low melting point materials (Schreiber et al., 2018; El-Zoka et al., 2020). By using this approach, we were able to successfully analyze the microporous, reduced iron that exhibits a bimodal pore distribution and obtain data on both the Fe and the filling material. APT analysis enables the identification of the structure and chemistry of the hydrogen-reduced Fe samples (Kim et al., 2021), including oxide inclusions, and provides a clear advantage in the identification of peaks in the mass spectra compared with C-based Pt or W precursors, for instance, that lead to a flurry of peaks as shown for instance in Barroo et al. (2020). Our approach to APT sample preparation allows to measure the atomic-level chemistry of not only nanoporous materials but also different structural materials. For instance, by implementing this technique, the dopant content inside a hollow electrode for Li-ion batteries (Wang et al., 2019; Liu et al., 2020) or elemental distributions at a stress/corrosion-induced crack inside a metal can be investigated (Razmpoosh et al., 2021).

## Materials and Methods

### Materials

A piece of  $5 \times 5 \times 0.5$  mm single crystalline, (100)-orientated FeO (wüstite, MaTech) was sliced into four pieces and 20 g of the as-received Bi-In-Sn fusible alloy (Field's metal, Alfa Aesar) was cut into a  $0.5 \times 1.0 \times 0.5$  cm piece. The sliced wüstite was first fabricated into an APT specimen followed by running APT measurements. The same sliced wüstite was then reduced in an in-house designed furnace with pure dihydrogen gas with a flow rate of 30 L/h at 700°C for 2 h.

### APT Specimen Preparation

For APT specimen preparation, we used an SEM-FIB FEI Helios Nanolab 600, equipped with a stage that can perform heating. The stage can also be cryogenically cooled by a cold gaseous nitrogen (Gatan C1001). Specimens from the wüstite before and after reduction were prepared using the lift-out protocol outlined in Thompson et al. (2007). All scanning electron micrographs were taken at 30 kV and 1.6 nA. A final annular ion-beam milling process at 30 kV and 48 pA was performed. A Ga-contamination cleaning protocol at 5 kV was not done on the fabricated APT specimens since a cryo-prepared sample has less critical issue with Ga implementation due to the anticipated decrease in Ga penetration rate (Thompson et al., 2007; Lilensten & Gault, 2020). Following heating to room temperature in the SEM-FIB, the APT specimens were taken out under ambient conditions and loaded inside a local electrode atom probe (LEAP) 5000 XS system (CAMECA). A specimen base temperature of 50 K, a pulse frequency of 100 kHz, a detection rate of 0.5%, and a pulse energy of 10 pJ were set for APT measurement. Cameca's Atom Probe Suite 6 was used for the 3D reconstructions and data analysis.

## Results

### Before and After H Reduction on a Single-Crystalline Wüstite

Figure 1a shows the morphology of the as-received wüstite sample. Following specimen preparation, the APT measurement was successful (Figs. 1b, 1c). The 3D atom map of a dataset from the wüstite is shown in Figure 1d. As expected, Fe and O are homogeneously distributed, and the atomic composition of Fe and O is 50.6 and 49.4 at%, respectively.

After the hydrogen reduction process of the wüstite, a sponge-like structure of iron is formed with large cracks and micron-sized open pores (Matthew et al., 1990), as shown in Figures 1e–1g. In our preliminary trials, the standard lift-out method is no longer applicable to fabricate needle-shaped APT specimens from the reduced iron, since there are too many defects with a critical size within the specimen's failure. The specimen itself cannot stand its own weight during the Ga-ion annular milling process and mechanically fails. When a specimen survived the preparation, voids and cracks cannot tolerate the field evaporation and eventually result in early fracture of the specimen in the atom probe.

### Encapsulation of Porous Sample with Bi-In-Sn Alloy and APT Specimen Preparation

To eliminate the risk of premature failures in APT measurement of porous reduced wüstite, the encapsulated specimen was fabricated as follows. First, the sliced fusible alloy is placed on a blank Si holder and tilted to 52° toward an e-beam column in the FIB to mill a clear pattern. Rectangular trenches ( $15 \times 3 \mu\text{m}^2$ ) are milled till 10  $\mu\text{m}$  in depths on the front and the back sides of the region of interest using a Ga-ion beam current of 2.8 nA at 30 kV. Because of ion-beam induced local heating and re-deposition, an uncontrollable milling behavior appears and, therefore, the trenches are uneven (Fig. 2a). The stage is then tilted back to 0° and the L-shape horizontal cut is made at the bottom of the lamella (Fig. 2b). The sample is lifted-out *in situ* using the micro-manipulator, and welding with Pt/C assisted by the Ga ion beam (Fig. 2c).

The sample is then dropped on to a commercial Cu clip (CAMECA). In order to prevent the spreading of the liquid metal droplet on the Cu clip, a trench ( $2 \times 15 \times 1 \mu\text{m}^3$ ) is milled as shown in Figure 2d. The lifted-out lamella is carefully attached on the side of the trench using FIB-Pt/C deposition (Figs. 2e–2g). Then, a lamella is lifted out of the reduced porous iron sample and the lamella is placed on top of the fusible alloy (Figs. 2h, 2i).

After the attachment, the Cu clip is taken out and the FIB stage is switched to the heating/cryo stage, and the sample remounted and imaged once again to ensure alignment. Using the temperature controller, the stage is heated up to melt the fusible alloy which has the melting point of 62°C. The lamella of the alloy gradually melts and subsequently becomes a droplet-like feature at 70°C (see Figs. 3a–3c). We let the liquid infiltrate the porous iron for approximately 5 min, and then the stage is cooled back down to room temperature.

Figures 3d and 3e show that cooling below the melting point of the fusible alloy leads to the solidification of the melt and the formation of a composite structure. The open micro-pores are filled with the Field's metal matrix. Figure 3f shows the cross-sectioning of the porous iron embedded in the fusible alloy matrix. The cross-sectional composite lamella is prepared with a lower ion-beam

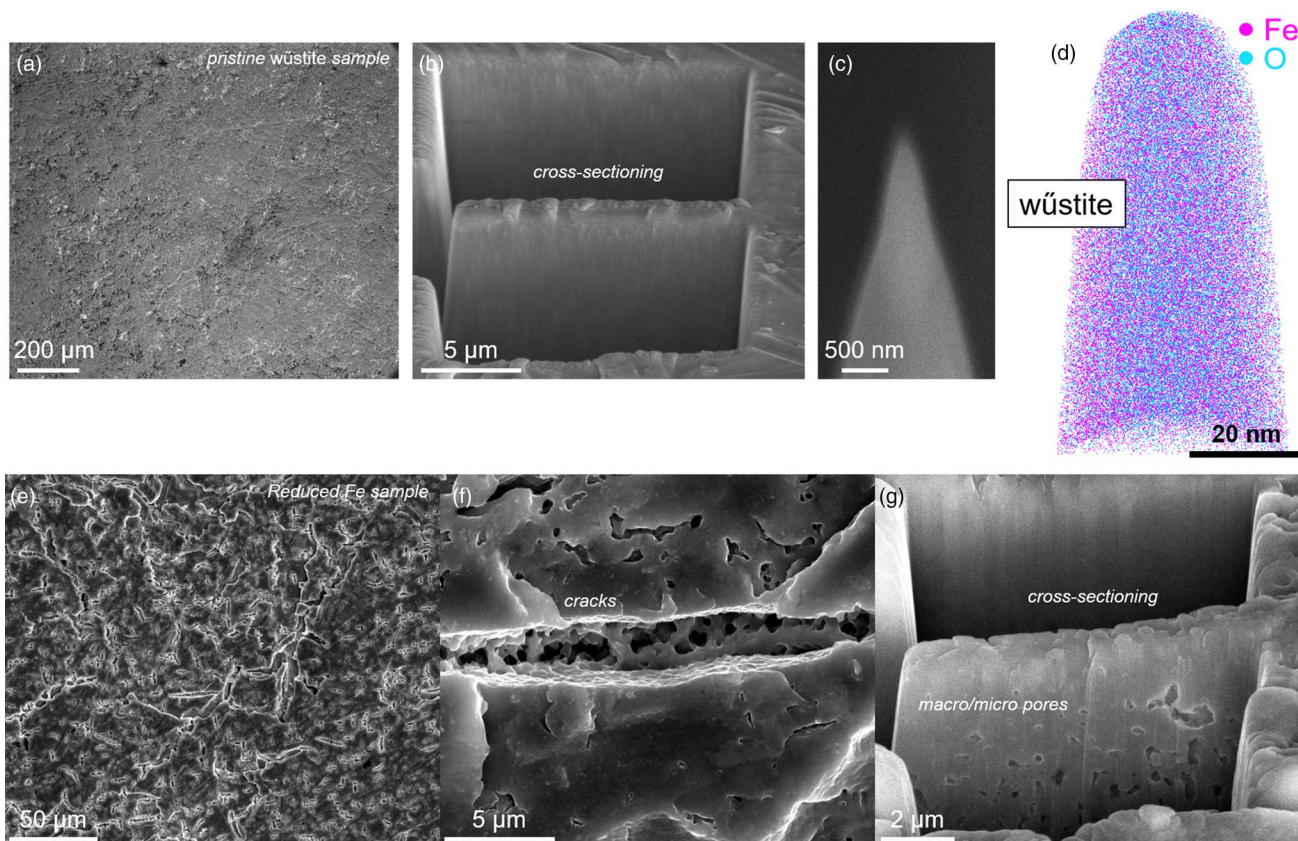


**Fig. 1.** Characterization on wüstite before and after H reduction. (a) Surface and (b) cross-sectional SEM images of as-received wüstite. (c) A final APT specimen of wüstite. (d) 3D atom map of wüstite from the acquired dataset. (e,f) Surface and (g) cross-sectional SEM images of as-reduced iron.

current (93 pA) to avoid potential melting. No open pores or cracks are observed in the SEM, and back-scattered electron (BSE) imaging showed no difference between the iron and the matrix (not shown here), indicating that the melted alloy filled the voids.

Kim et al. (2019) reported uncontrollable Ga-ion milling behavior when the diameter of the fusible alloy is less than 1  $\mu\text{m}$  due to the size-dependent reduction of the melting temperature; therefore, after the composite sample is mounted on a commercial Si micro-tip coupon, the stage is cooled to cryogenic temperature, at  $-190^\circ\text{C}$ , to avoid the melting of the Field's metal within the needles (Fig. 4a). Figures 4b and 4c show the controlled ion milling, which is performed at 30 kV and 48 pA. Overall, with this approach, a porous sample difficult to analyze by APT was fabricated into a dense needle-shaped specimen suitable for APT.

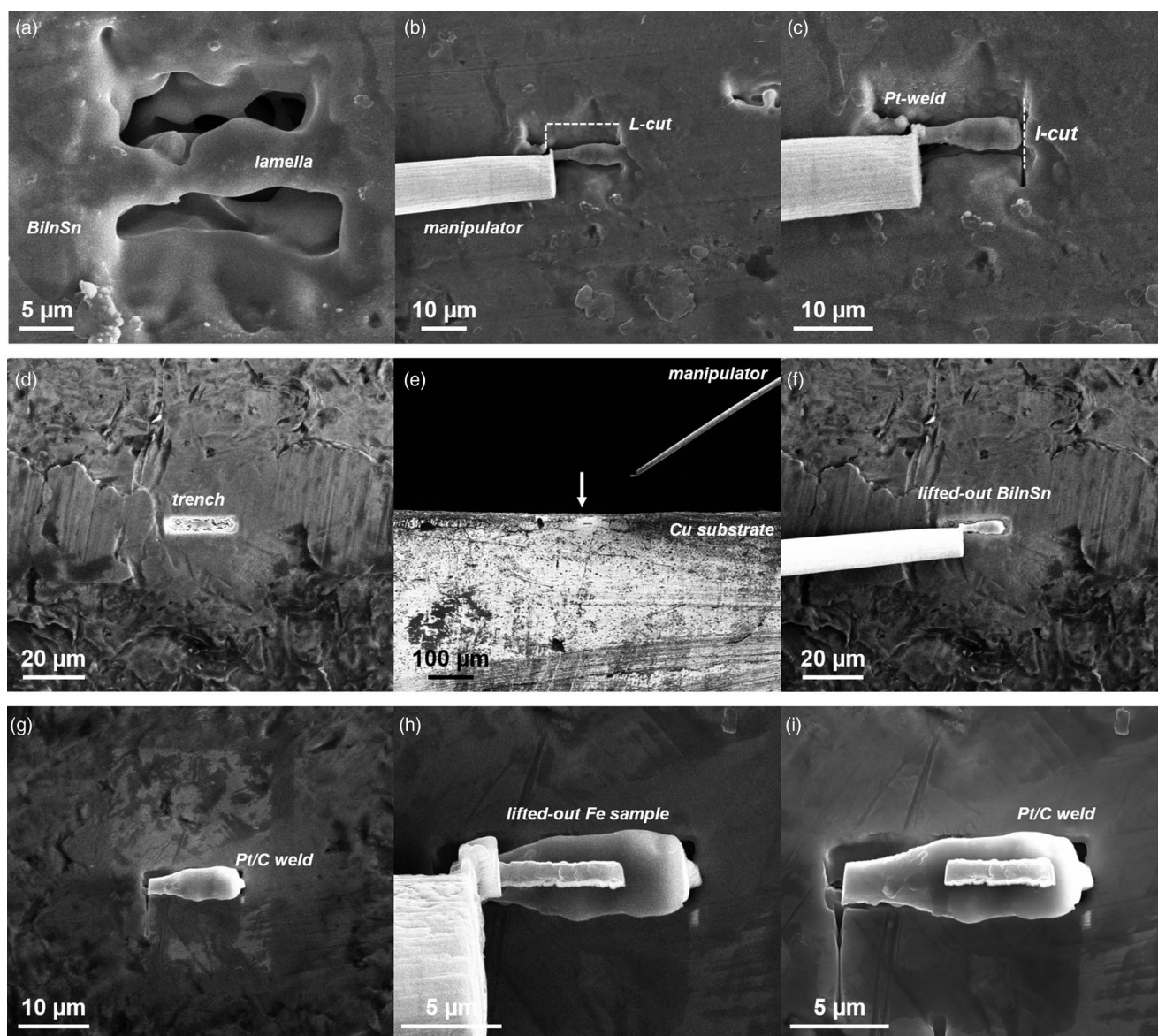
### APT Analysis

Figure 5a shows the 3D atom map acquired from the reduced iron. The detected atomic composition is 99.87 at% Fe and 0.13 at% O, indicating that most of O were removed by the hydrogen reduction process, even in the middle of the Fe-ligaments. From the 2D contour map of Fe, calculated within the cyan, cuboidal region-of-interest, a clear pattern showing the (011) pole and (020) pole indicates that the reduced sample has a non-amorphous body-centered cubic structure that corresponds to  $\alpha$ -Fe. No constituent elements of the fusible alloy are detected which implies that the liquid metal penetration does not proceed into the iron, as expected.

Within the  $\alpha$ -Fe, interestingly, an oxide particle is detected as shown in Figure 5b. Although the as-received sample was manufactured in a laboratory by the Czorslaski process, it still contained impurities such as Mg and Ca which are commonly known as gangue elements in an iron ore (Kim et al., 2021). In the  $\alpha$ -Fe, these impurities are in a precipitate-like feature with a diameter of approximately 4 nm. During the H-reduction process, gangue oxide cannot be reduced and impurities that cannot be expelled from the metal at the reduction front are trapped inside the  $\alpha$ -Fe, forming small particles. On the macro scale, CaO was reported to have no significant effect on the reduction kinetics (Turkdogan & Vinters, 1971; Turkdogan et al., 1971), whereas reduction was found to be accelerated by MgO (Chen et al., 2019). Chemical probing and nanostructural analysis using APT could reveal the presence of these impurity oxides and provide valuable information helping to understand the effects of nanostructure and nanochemistry of the iron ores on the efficient production of greener steel.

It is reported that the Bi-In-Sn alloy has three distinctive phases, namely  $\text{BiIn}_2$ ,  $\text{In}_2\text{Sn}_9$ , and  $\text{In}_3\text{Sn}$ . Here, in Figure 5c, the 3D atom map of the fusible alloy shows a homogeneous elemental distribution and the composition is 91.92, 8.06 and 0.02 at% for Sn, In, and Bi, respectively, which corresponds to the  $\text{In}_2\text{Sn}_9$  phase. Within the matrix, no iron-related peak nor impurities oxide peaks from the porous iron are detected, allowing us to confirm that no galvanic replacement happened during the sample preparation.

Even though no low energy Ga cleaning was performed for these specimens, the  $\alpha$ -Fe and the Field's metal contain less



**Fig. 2.** A lifted-out Bi–In–Sn alloy and porous iron on a Cu clip before *in situ* heating and cooling process. (a) The Bi–In–Sn alloy before lift-out. (b) L-horizontal cut is made and a micro-manipulator is inserted to lift the lamella. (c) I-vertical cut releases the lamella from the bulk. (d) A prior trench on the Cu clip. (e) A manipulator with the sample attached is inserted. (f,g) The lamella is mounted on a Cu trench. (h) The porous Fe lamella is mounted on the top. (i) The stacked sample before heating process.

than 0.16 and 0.25 at% Ga, respectively. The Ga implantation was reported to be low, owing to the low temperatures used during final stages of sample preparation. The interaction and diffusion rate of Ga into the specimen are decreased at lower temperatures (Lilensten & Gault, 2020).

### Summary and Discussion

To summarize, the overall process for filling voids in porous materials using fusible alloys are schematically shown in Figure 6. First, a trench was milled on the Cu clip to load the lifted-out fusible alloy and subsequently, the porous material. The lift-out process was performed according to Miller et al. (2007) and Thompson et al. (2007). The stage temperature was first raised up to 70°C in order to melt the fusible alloy. After the stacked samples are mixed into a single composite, the stage

is cooled down to room temperature. After solidification of the molten metal, a region of interest was extracted using the micro-manipulator and attached to a Si support using ion-beam induced Pt/C deposition. Once the sliced samples were attached onto the pillar, the stage was cooled down to cryogenic temperature (approx. –190°C) to avoid ion-beam induced melting of the Field's metal.

The combination of *in situ* FIB heating and cooling, combined with a liquid metal yields a versatile approach to infiltrate and encapsulate micro-to-nanoporous materials, thus enabling APT measurement successfully. An advantage of this method is that the encapsulating material is conductive. According to Seol et al. (2016), the surface modification from the conductive layer coating improves the overall evaporation sequences. Unlike ceramic coating approaches (Sundell et al., 2019; Webel et al., 2021), a high quality data could be acquired here because a fusible

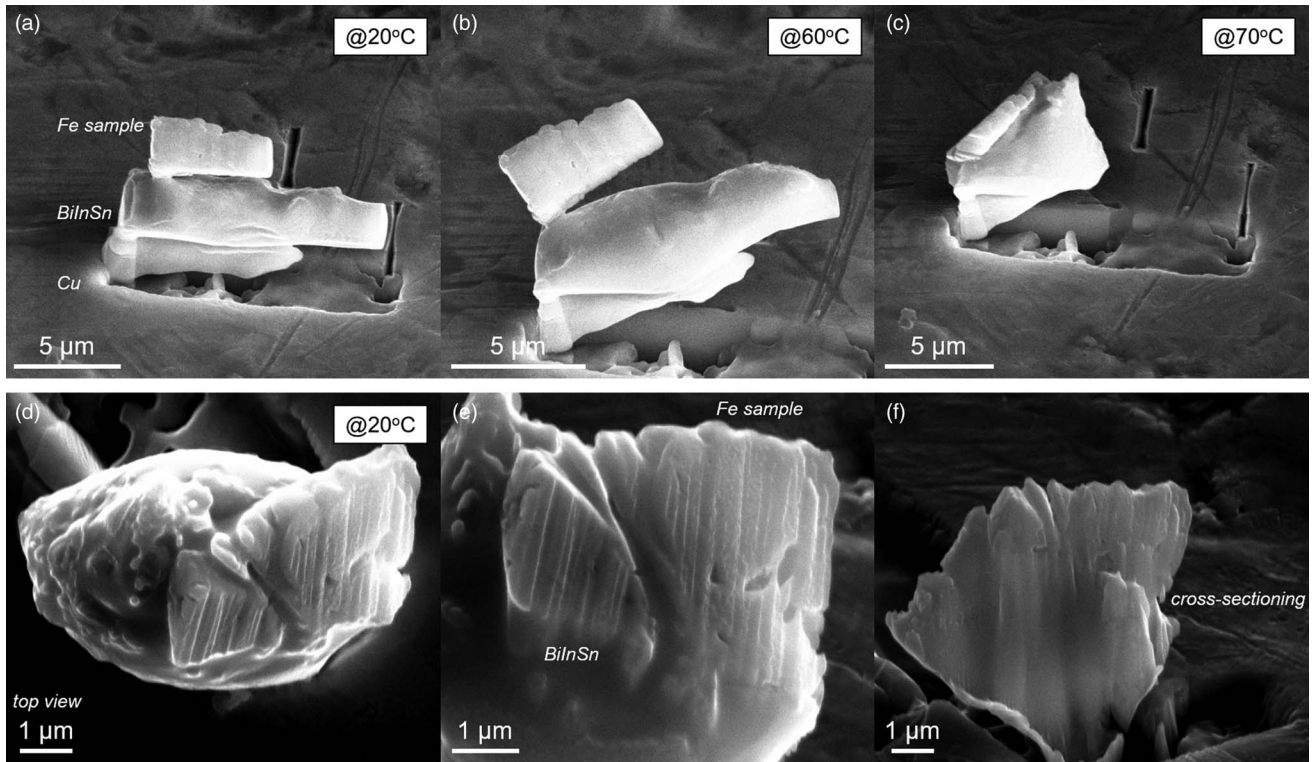


Fig. 3. *In situ* experiment: (a–c) heating up to 70°C and (d–f) cooling back to 20°C.

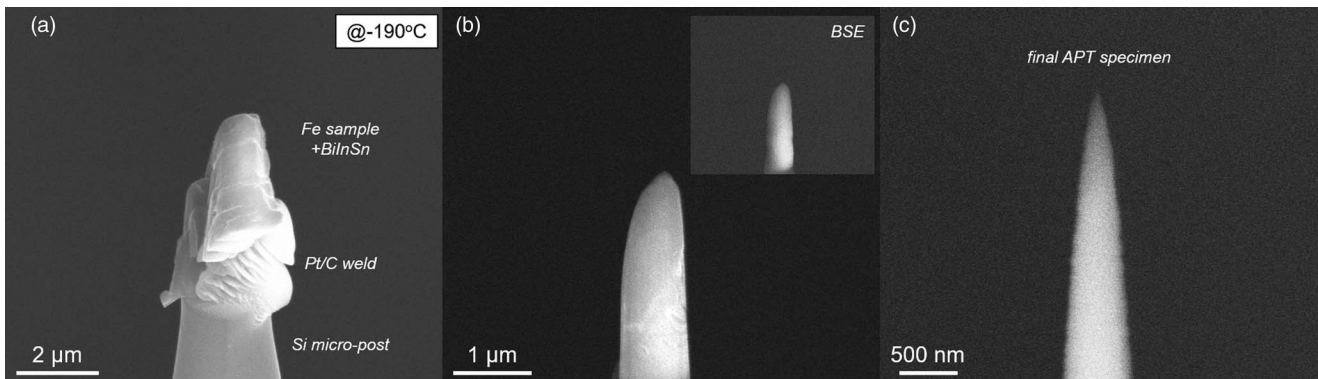


Fig. 4. *In situ* cryogenic annular milling of the composite. (a) The specimen post is cooled down to cryogenic temperature. (b) After a rough annular FIB milling step. Inset shows BSE image of the specimen. (c) A final APT specimen milled at cryogenic temperature.

alloy has relatively high thermal (0.19 W/cm °C) and electrical conductivity (0.57 nΩ m) which allows to dissipate the energy and electrons quickly to the base of the specimen (Lipchitz et al., 2015). This can explain the high (3:3) success rate of sample preparation in this investigation, with over 10 million ions collected for each specimen, and without premature or microfractures. A difficulty with this protocol is to position the material of interest toward the specimen's apex, otherwise only the matrix is collected during the atom probe measurement.

Development and use of other low melting point alloys for encapsulation could be very beneficial to further optimize this method. One of the main criteria to be taken into consideration is that none of the metals in the alloy are miscible with the

material to be analyzed. This was the case for Fe and BiSnIn (von Goldbeck, 1982a, 1982b, 1982c). The melting point of BiSnIn is also suitable in our case so as not to coarsen the porous structure. We imagine that a dip-coating process can be performed for aggregated powder in the future using a suitable liquid metal. After lifting the interested lamella, the sample can be immersed in a preheated liquid metal and it allows penetrates pores or spaces inside (see Fig. 7).

To preserve the initial state of nanoporous materials, non-chemical interaction and low-temperature range operation should be considered in APT sample preparation. For example, an Au nanoporous metal is sensitive to heat and when the temperature increases, its structure changes due to coarsening (Hakamada &

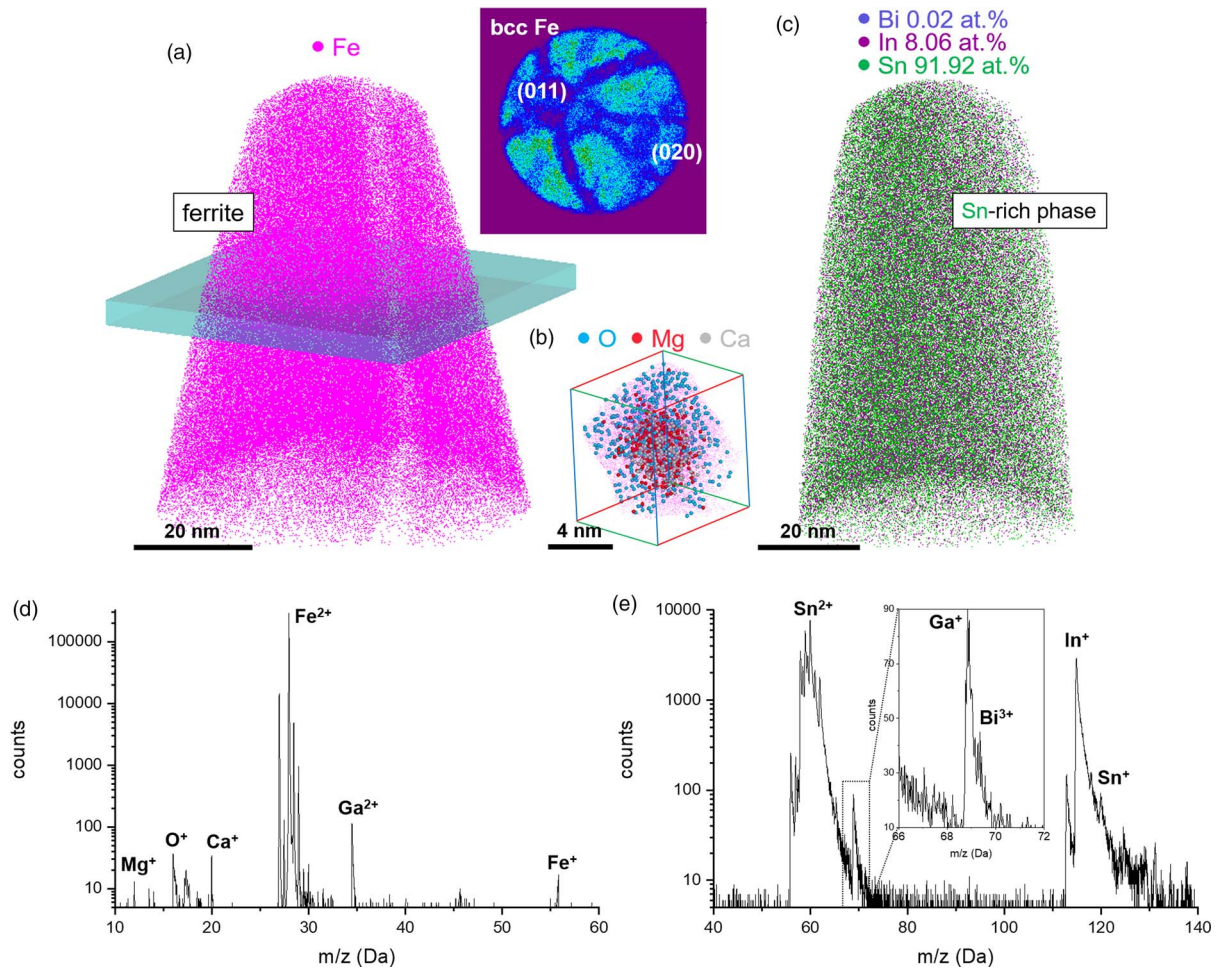


**Fig. 5.** (a) 3D atom map of the  $\alpha$ -Fe sample. Pink dots represent reconstructed Fe atoms. Inset shows 2D desorption map histogram of Fe with crystallographic pole features. (b) Extracted atom map of impurity oxide region. Blue, red, and gray dots represent reconstructed O, Mg, and Ca atoms (a). (c) 3D atom map of the Bi-In-Sn alloy. Blue-gray, purple, and Green represent reconstructed Bi, In, and Sn atoms. Mass spectra from (d) the  $\alpha$ -Fe and (e) the Bi-In-Sn alloy 3D atom maps.

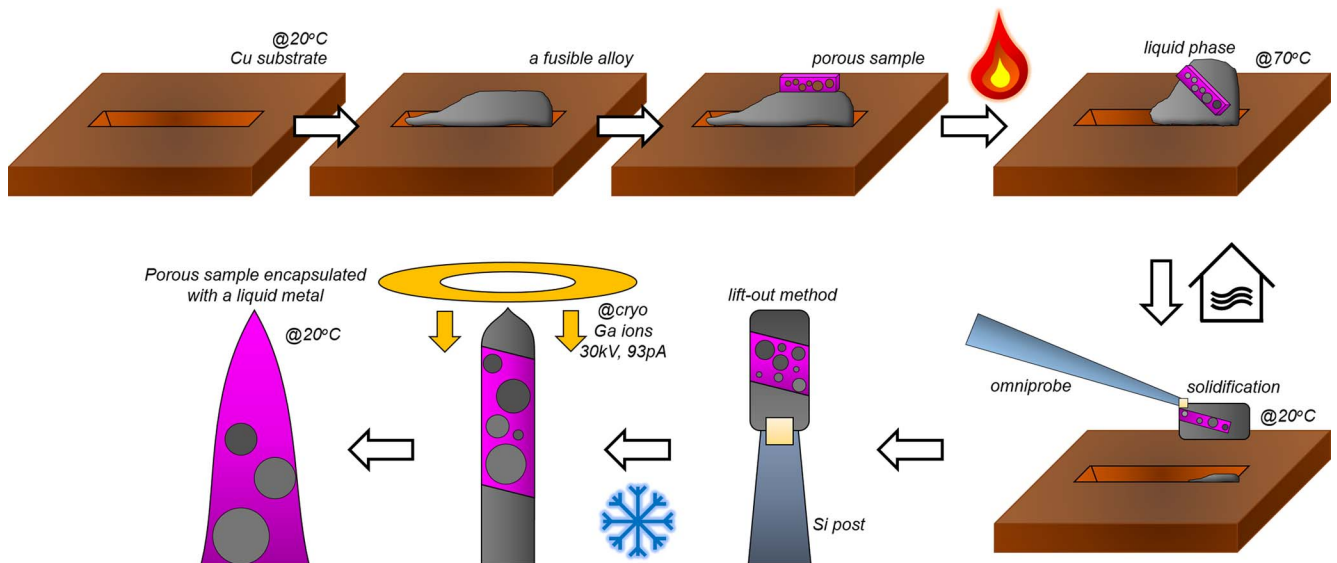


**Fig. 6.** A schematic illustration of encapsulation of porous sample in a fusible alloy.

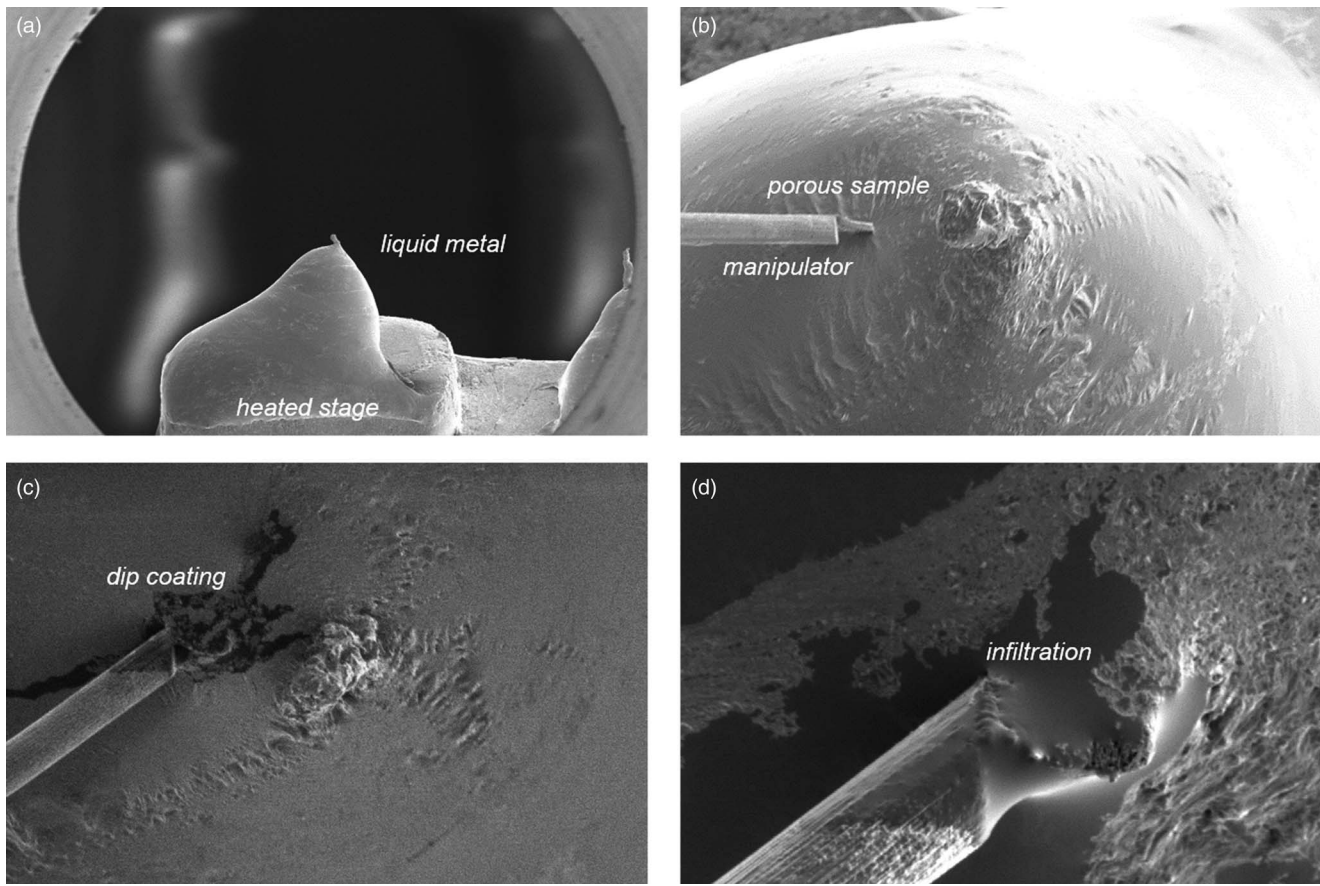


Fig. 7. A modified encapsulating approach for a porous nanomaterial using a liquid metal.

Mabuchi, 2009; El-Zoka et al., 2018a). The well-known atomic layer deposition encapsulation technique could not be applied in such a system since its operating temperature is often above 200°C (Johnson et al., 2014) and introduces carbon contaminants from organic precursors that could change the evaporation field of the specimen and the chemical composition analysis (Choi et al., 2013).

## Conclusion

Due to the difficulty of applying APT to porous materials, their near-atomic-scale compositional distribution remains elusive. We have demonstrated a new method for preparing APT specimens from a sample containing micro- to nanopores. A sponge-like iron sample prepared by hydrogen reduction from a single crystal of wüstite was infiltrated and embedded in a fusible Bi–In–Sn alloy. The complete encapsulation was achieved by melting and solidifying the alloy using an *in situ* SEM-FIB. No corrosion or dissolution in the sample was observed during the sample preparation and high-quality APT data were collected. This approach allows to explore a variety of porous materials using APT, including noble metals such as nanoporous Au but also nanoporous W, Re, Mo, and Raney Ni. There is also a range of fusible alloys (e.g., eutectic Ga–In alloy) beyond Field’s metal (Yatsenko et al., 2008; Chang et al., 2018) that could be used depending on the melting point and susceptibility to cause corrosion. To conclude, liquid metal encapsulation makes a range of complex nanostructured materials amenable to APT analysis.

**Acknowledgments.** The authors are grateful to Uwe Tezins, Andreas Sturm, and Christian Broß for their support to the APT and FIB facilities. We also thank Dr. Xue Zhang, Dr. Michael Rohwerder, and Dr. Dierk Raabe for providing samples and collaborating on the direct-hydrogen reduction of iron ore project. S.-H.K., A.E.-Z., and B.G. acknowledge financial support from the ERC-CoG-SHINE-771602.

## References

- Barroo C, Akey AJ & Bell DC (2019). Atom probe tomography for catalysis applications: A review. *Appl Sci* **9**, 2721.
- Barroo C, Akey AJ & Bell DC (2020). Aggregated nanoparticles: Sample preparation and analysis by atom probe tomography. *Ultramicroscopy* **218**, 113082.
- Chang H, Guo R, Sun Z, Wang H, Hou Y, Wang Q, Rao W & Liu J (2018). Direct writing and repairable paper flexible electronics using nickel–liquid metal Ink. *Adv Mater Interfaces* **5**, 1800571. doi:10.1002/admi.201800571.
- Chang Y, Lu W, Guérolé J, Stephenson LT, Szczpaniak A, Kontis P, Ackerman AK, Dear F, Mouton I, Zhong X, Raabe D, Gault B, Zhang S, Dye D, Liebscher CH, Ponge D, Korte-Kerze S, Raabe D & Gault B (2019). Ti and its alloys as examples of cryogenic focused ion beam milling of environmentally-sensitive materials. *Nat Commun* **10**, 942.
- Chen Z, Zeilstra C, van der Stel J, Sietsma J & Yang Y (2019). Review and data evaluation for high-temperature reduction of iron oxide particles in suspension. *Ironmak Steelmak*, 1–7. doi:10.1080/03019233.2019.1589755.
- Choi M, Lyons JL, Janotti A & Van de Walle CG (2013). Impact of carbon and nitrogen impurities in high- $\kappa$  dielectrics on metal-oxide-semiconductor devices. *Appl Phys Lett* **102**, 142902. doi:10.1063/1.4801497.
- Dantas De Moraes L, Chevalliez S & Mouleres S (2014). Low temperature FIB cross section: Application to indium micro bumps. *Microelectron Reliab* **54**, 1802–1805.

- De Geuser F & Gault B (2020). Metrology of small particles and solute clusters by atom probe tomography. *Acta Mater* **188**, 406–415.
- El-Zoka AA, Howe JY, Newman RC & Perovic DD (2018a). In situ STEM/SEM study of the coarsening of nanoporous gold. *Acta Mater* **162**, 67–77.
- El-Zoka AA, Kim S-H, Deville S, Newman RC, Stephenson LT & Gault B (2020). Enabling near-atomic-scale analysis of frozen water. *Sci Adv* **6**, eabd6324.
- El-Zoka AA, Langelier B, Botton GA & Newman RC (2017). Enhanced analysis of nanoporous gold by atom probe tomography. *Mater Charact* **128**, 269–277.
- El-Zoka AA, Langelier B, Korinek A, Botton GA & Newman RC (2018b). Advances in nanoscale characterization of refined nanoporous gold. *Electrochim Acta* **283**, 611–618.
- El-Zoka AA, Langelier B, Korinek A, Botton GA & Newman RC (2018c). Nanoscale mechanism of the stabilization of nanoporous gold by alloyed platinum. *Nanoscale* **10**, 4904–4912.
- Felfer P, Benndorf P, Masters A, Maschmeyer T & Cairney JM (2014). Revealing the distribution of the atoms within individual bimetallic catalyst nanoparticles. *Angew Chem Int Ed* **53**, 11190–11193.
- Felfer P, Li T, Eder K, Galinski H, Magyar AP, Bell DC, Smith GDW, Kruse N, Ringer SP & Cairney JM (2015). New approaches to nanoparticle sample fabrication for atom probe tomography. *Ultramicroscopy* **159**, 413–419.
- Gault B, Chiamonti A, Cojocaru-Mirédin O, Stender P, Dubosq R, Freysoldt C, Makineni SK, Li T, Moody M & Cairney JM (2021). Atom probe tomography. *Nat Rev, Methods Primers* **1**, 1–51.
- Gault B, Moody MP, Cairney JM & Ringer SP (2012). Atom probe crystallography. *Mater Today* **15**, 378–386.
- Hakamada M & Mabuchi M (2009). Thermal coarsening of nanoporous gold: Melting or recrystallization. *J Mater Res* **24**, 301–304.
- Jenkins BM, Danoix F, Gouné M, Bagot PAJ, Peng Z, Moody MP & Gault B (2020). Reflections on the analysis of interfaces and grain boundaries by atom probe tomography. *Microsc Microanal* **26**, 247–257.
- Johnson RW, Hultqvist A & Bent SF (2014). A brief review of atomic layer deposition: From fundamentals to applications. *Mater Today* **17**, 236–246.
- Kim SH, Lee JY, Ahn JP & Choi PP (2019). Fabrication of atom probe tomography specimens from nanoparticles using a fusible Bi-In-Sn alloy as an embedding medium. *Microsc Microanal* **25**, 438–446.
- Kim S-H, Kang PW, Park OO, Seol J-B, Ahn J-P, Lee JY & Choi P-P (2018). A new method for mapping the three-dimensional atomic distribution within nanoparticles by atom probe tomography (APT). *Ultramicroscopy* **190**, 30–38.
- Kim S-H, Lim J, Sahu R, Kasian O, Stephenson LT, Scheu C & Gault B (2020). Direct imaging of dopant and impurity distributions in 2D MoS<sub>2</sub>. *Adv Mater* **32**, 1907235.
- Kim S-H, Zhang X, Ma Y, Souza Filho IR, Schweinar K, Angenendt K, Vogel D, Stephenson LT, El-Zoka AA, Mianroodi JR, Rohwerder M, Gault B & Raabe D (2021). Influence of microstructure and atomic-scale chemistry on the direct reduction of iron ore with hydrogen at 700°C. *Acta Mater* **212**, 116933.
- Larson D, Prosa T & Kelly T (2013). *Local Electrode Atom Probe Tomography - A user's guide*, 1st ed. New York: Springer, Verlag. doi: 10.1007/978-1-4614-8721-0.
- Larson DJ, Giddings AD, Wu Y, Verheijen MA, Prosa TJ, Roozeboom F, Rice KP, Kessels WMM, Geiser BP & Kelly TF (2015). Encapsulation method for atom probe tomography analysis of nanoparticles. *Ultramicroscopy* **159**, 420–426.
- Li T, Bagot PAJ, Christian E, Theobald BRC, Sharman JDB, Ozkaya D, Moody MP, Tsang SCE & Smith GDW (2014). Atomic imaging of carbon-supported Pt, Pt/Co, and Ir@Pt nanocatalysts by atom-probe tomography. *ACS Catal* **4**, 695–702.
- Lilensten L & Gault B (2020). New approach for FIB-preparation of atom probe specimens for aluminum alloys. *PLoS One* **15**, e0231179.
- Lim J, Kim S-H, Aymerich Armengol R, Kasian O, Choi P-P, Stephenson LT, Gault B & Scheu C (2020). Atomic-scale mapping of impurities in partially reduced hollow TiO<sub>2</sub> nanowires. *Angew Chem Int Ed* **59**, 5651–5655. doi:10.1002/anie.201915709
- Lipchitz A, Harvel G & Sunagawa T (2015). Experimental investigation of the thermal conductivity and viscosity of liquid In-Bi-Sn eutectic alloy (Field's metal) for use in a natural circulation experiential loop. In *Proceedings, ICONE International Conference on Nuclear Engineering*.
- Liu H, Chen Y, Jiang B, Zhao Y, Guo X & Ma T (2020). Hollow-structure engineering of a silicon-carbon anode for ultra-stable lithium-ion batteries. *Dalton Trans* **49**, 5669–5676. doi:10.1039/D0DT00566E.
- Lyon SB (2010). Corrosion of carbon and low alloy steels. In *Shreir's Corrosion*, Vol. 3, pp. 1693–1736. Elsevier.
- Matthew SP, Cho TR & Hayes PC (1990). Mechanisms of porous iron growth on wustite and magnetite during gaseous reduction. *Metall Trans B* **21**, 733–741.
- Meisnar M, Moody M & Lozano-Perez S (2015). Atom probe tomography of stress corrosion crack tips in SUS316 stainless steels. *Corros Sci* **98**, 661–671.
- Miller MK & Forbes RG (2009). Atom probe tomography. *Mater Charact* **60**, 461–469.
- Miller MK, Russell KF, Thompson K, Alvis R & Larson DJ (2007). Review of atom probe FIB-based specimen preparation methods. *Microsc Microanal* **13**, 428–436.
- Mouton I, Printemps T, Grenier A, Gambacorti N, Pinna E, Tiddia M, Vacca A & Mula G (2017). Toward an accurate quantification in atom probe tomography reconstruction by correlative electron tomography approach on nanoporous materials. *Ultramicroscopy* **182**, 112–117.
- Nishikawa O, Taniguchi M, Watanabe S, Yamagishi A & Sasaki T (2006). Scanning atom probe study of dissociation of organic molecules on titanium oxide. *Jpn J Appl Phys* **45**, 1892–1896.
- Perea DE, Liu J, Bartrand J, Dicken Q, Thevuthasan ST, Browning ND & Evans JE (2016). Atom probe tomographic mapping directly reveals the atomic distribution of phosphorus in resin embedded ferritin. *Sci Rep* **6**, 22321.
- Pfeiffer B, Erichsen T, Epler E, Volkert CA, Trompenaars P & Nowak C (2015). Characterization of nanoporous materials with atom probe tomography. *Microsc Microanal* **21**, 557–563.
- Prosa T, Kostrna Keeney S & Kelly TF (2010). Local electrode atom probe analysis of poly(3-alkylthiophene)s. *J Microsc* **237**, 155–167.
- Razmpoosh MH, Langelier B, Marzbanrad E, Zurob HS, Zhou N & Biro E (2021). Atomic-scale investigation of liquid-metal-embrittlement crack-path: Revealing mechanism and role of grain boundary chemistry. *Acta Mater* **204**, 116519.
- Rivas NA, Babayigit A, Conings B, Schwarz T, Sturm A, Manjón AG, Cojocaru-Mirédin O, Gault B & Renner FU (2020). Cryo-focused ion beam preparation of perovskite based solar cells for atom probe tomography. *PLoS One* **15**, e0227920.
- Schreiber DK, Perea DE, Ryan JV, Evans JE & Vienna JD (2018). A method for site-specific and cryogenic specimen fabrication of liquid/solid interfaces for atom probe tomography. *Ultramicroscopy* **194**, 89–99.
- Seol JB, Kwak CM, Kim YT & Park CG (2016). Understanding of the field evaporation of surface modified oxide materials through transmission electron microscopy and atom probe tomography. *Appl Surf Sci* **368**, 368–377.
- Sundell G, Hulander M, Pihl A & Andersson M (2019). Atom probe tomography for 3D structural and chemical analysis of individual proteins. *Small* **15**, 1900316.
- Taylor SD, Liu J, Zhang X, Arey BW, Kovarik L, Schreiber DK, Perea DE & Rosso KM (2019). Visualizing the iron atom exchange front in the Fe (II)-catalyzed recrystallization of goethite by atom probe tomography. *Proc Natl Acad Sci USA* **116**, 2866–2874.
- Thompson K, Lawrence D, Larson DJ, Olson JD, Kelly TF & Gorman B (2007). In situ site-specific specimen preparation for atom probe tomography. *Ultramicroscopy* **107**, 131–139.
- Turkdogan ET, Olsson RG & Vinters JV (1971). Gaseous reduction of iron oxides: Part II. Pore characteristics of iron reduced from hematite in hydrogen. *Metall Mater Trans B* **2**, 3189–3196. doi:10.1007/BF02814971.
- Turkdogan ET & Vinters JV (1971). Gaseous reduction of iron oxides: Part I. Reduction of hematite in hydrogen. *Metall Mater Trans B* **2**, 3175–3188. doi:10.1007/BF02814970.
- von Goldbeck OK (1982a). Iron-Tin Fe-Sn. In *IRON—Binary Phase Diagrams*, pp. 139–142. Berlin, Heidelberg: Springer. <https://doi.org/10.1007/978-3-662-08024-5>.



- von Goldbeck OK** (1982b). Fe–Bi Iron–Bismuth. In *IRON—Binary Phase Diagrams*. pp. 22–23. Berlin, Heidelberg: Springer. <https://doi.org/10.1007/978-3-662-08024-5>.
- von Goldbeck OK** (1982c). Iron–Indium Fe–In. In *IRON—Binary Phase Diagrams*. pp. 53–55. Berlin, Heidelberg: Springer. <https://doi.org/10.1007/978-3-662-08024-5>.
- Wang C, Zhang L, Al-Mamun M, Dou Y, Liu P, Su D, Wang G, Zhang S, Wang D & Zhao H** (2019). A hollow-shell structured  $V_2O_5$  electrode-based symmetric full Li-Ion battery with highest capacity. *Adv Energy Mater* **9**, 1900909. doi:10.1002/aenm.201900909.
- Wang X, Hatzoglou C, Sneed B, Fan Z, Guo W, Jin K, Chen D, Bei H, Wang Y, Weber WJ & Zhang Y** (2020). Interpreting nanovoids in atom probe tomography data for accurate local compositional measurements. *Nat Commun* **11**, 1–11.
- Webel J, Weber L, Vardo E, Britz D, Kraus T & Mücklich F** (2021). Particle encapsulation techniques for atom probe tomography of precipitates in microalloyed steels. *Ultramicroscopy* **223**, 113219.
- Yang Q, Danaie M, Young N, Broadley V, Joyce DE, Martin TL, Marceau E, Moody MP & Bagot PAJ** (2019). Atom probe tomography of Au–Cu bimetallic nanoparticles synthesized by inert gas condensation. *J Phys Chem C* **123**, 26481–26489. doi:10.1021/acs.jpcc.9b09340.
- Yatsenko SP, Sabirzyanov NA & Yatsenko AS** (2008). Dissolution rates and solubility of some metals in liquid gallium and aluminum. *J Phys: Conf Series* **98**, 62032. doi:10.1088/1742-6596/98/6/062032.